Suppression of magnetic ordering in Fe-deficient $Fe_{3-x}GeTe_2$ from application of pressure

Dante J. O'Hara,[1,2,*,†] Zachary E. Brubaker,[2,3,5] Ryan L. Stillwell,[2] Earl F. O'Bannon,[2] Alexander A. Baker,[2] Daniel Weber,[4] Leonardus Bimo Bayu Aji,[2] Joshua E. Goldberger,[4] Roland K. Kawakami,[1,4] Rena J. Zieve,[5] Jason R. Jeffries,[2] and Scott K. McCall[2]

[1]*Materials Science and Engineering, University of California, Riverside, Riverside, California 92521, USA*
[2]*Lawrence Livermore National Laboratory, Livermore, California 94550, USA*
[3]*Oak Ridge National Laboratory, Oak Ridge, Tennessee 37831, USA*
[4]*The Ohio State University, Columbus, Ohio 43210, USA*
[5]*University of California, Davis, California 95616, USA*

(Received 29 April 2020; revised 12 July 2020; accepted 14 July 2020; published 3 August 2020)

Two-dimensional van der Waals magnets with multiple functionalities are becoming increasingly important for emerging technologies in spintronics and valleytronics. Application of external pressure is one method to cleanly explore the underlying physical mechanisms of the intrinsic magnetism. In this paper, the magnetic, electronic, and structural properties of van der Waals-layered, Fe-deficient $Fe_{3-x}GeTe_2$ are investigated. Magnetotransport measurements show a monotonic decrease in the Curie temperature (T_C) and the magnetic moment with increasing pressure up to 13.9 GPa. The electrical resistance of $Fe_{3-x}GeTe_2$ shows a change from metallic to a seemingly nonmetallic behavior with increasing pressure. High-pressure angle dispersive powder x-ray diffraction shows a monotonic compression of the unit cell and a reduction of the volume by ∼25% with no evidence of structural phase changes up to 29.4(4) GPa. We suggest that the decrease in the T_C due to pressure results from increased intralayer coupling and delocalization that leads to a change in the exchange interaction.

DOI: 10.1103/PhysRevB.102.054405

I. INTRODUCTION

The discovery of intrinsic ferromagnetism in the monolayer limit of van der Waals (vdW) materials has resulted in many opportunities to study quasi-two-dimensional (2D) magnetism [1,2]. Properties, such as gate-tunable magnetism and giant tunneling magnetoresistance have been observed in mechanically exfoliated CrI_3 [2–5], and room-temperature ferromagnetic ordering in large-area films of monolayer $MnSe_2$ and VSe_2 have been reported, showing potential for spin-based technological applications [6,7]. Among the 2D magnets, $Fe_{3-x}GeTe_2$ is of interest because of its high Curie temperature, T_C, strong perpendicular magnetic anisotropy, and competing magnetic phases, all of which are tunable by controlling the concentration of Fe and the number of layers [8–15]. Measurements of the bulk parent compound may provide a better understanding of the single atomic sheets of these chalcogen-based vdW materials as well as key insights needed to develop more structurally and magnetically stable 2D materials.

"Chemical pressure," generated by substituting Ni or Co into the Fe sites, has been shown to suppress ferromagnetism in $Fe_{3-x}GeTe_2$ crystals [16,17]. Pressure offers a clean approach to modifying the relative strengths of the exchange interactions by altering the interatomic separations of the atomic planes without changing the chemical composition [18,19]. For example, hydrostatic pressure drives a spin-reorientation transition in vdW $Cr_2Ge_2Te_6$ by reducing the Cr-Te bond distance within individual unit layers, therefore, changing the spin-orbit interaction [20].

Here, we investigate the crystal structure, electronic, and magnetic properties of Fe-deficient $Fe_{3-x}GeTe_2$ as a function of temperature and pressure and observe a reduction of T_C with increasing pressure up to 13.9 GPa. Independent determinations of T_C based on temperature-dependent measurements of magnetization, resistance (R_{xx}), and anomalous Hall effect (AHE) provide consistent values of T_C and confirm the pressure dependence of T_C. Pressure-dependent x-ray diffraction (XRD) provides a correlation of T_C with the lattice parameters a (in-plane) and c (out-of-plane), yielding trends for Fe-deficient $Fe_{2.75}GeTe_2$ that are similar to previous results on stoichiometric Fe_3GeTe_2 [21]. This paper indicates that the structure can be controlled with pressure, systematically suppressing the magnetic ordering of $Fe_{3-x}GeTe_2$ until no longer detectable near 16 GPa.

II. METHODS

Crystals of Fe-deficient $Fe_{2.75}GeTe_2$ were grown from a Te flux using a technique adapted from previous reports [15]. Initial ingredients of 80.4-mg Fe granules (2 equivalent (eq.), 99.98% purity, Alfa Aesar), 52.3-mg Ge powder (1 eq., 99.999% purity, Alfa Aesar), and 367.4-mg Te lumps (4 eq., 99.999% purity, Alfa Aesar) were heated in an alumina crucible in an evacuated quartz ampoule to 950 °C, soaked for 12 h, cooled to 875 °C at a rate of 60 °C/h, and to 675 °C

*Corresponding author: dante.ohara.ctr@nrl.navy.mil
†D. J. O'Hara is currently with the U.S. Naval Research Laboratory, Materials Science and Technology Division, U.S. Naval Research Laboratory, 4555 Overlook Ave. SW, Washington, D.C. 20375.

at a rate of 3 °C/h. The ampoule was quenched to air, and the hot flux removed by centrifugation, yielding metallic millimeter-sized crystals. Sample composition of a Fe:Ge:Te ratio of 2.75:1:2 was confirmed by Rutherford backscattering measurements (Appendix Fig. 7).

The ambient lattice parameters of the samples were measured using a Bruker D8 Discover x-ray diffractometer with a Cu $K\alpha$ source ($\lambda = 1.5406$ Å). Pressure-dependent angle dispersive x-ray diffraction scans were performed at sector 16-BMD of the Advanced Photon Source at Argonne National Laboratory using synchrotron radiation monochromated by Si(111) to a wavelength of 0.4133 Å (30 keV). Detector orientation, distance, and x-ray wavelength were calibrated using a National Institute of Standards and Technology CeO_2 powder sample. Samples were powdered and loaded into a Lawrence Livermore National Laboratory (LLNL) membrane diamond-anvil cell (DAC) [22], a rhenium gasket was used to contain the sample, and neon was used as the pressure-transmitting medium. The pressure was estimated by measuring the lattice parameter of Au powder, which was mixed with the sample, using the Au equation of state published by Fei *et al.* [23]. At select pressures, ruby fluorescence spectra were collected, and the pressure was estimated by using the ruby calibration of Dewaele *et al.* [24]. The XRD patterns were collected by an area detector and radially integrated into powder patterns using DIOPTAS [25]. The CeO_2 diffraction pattern at ambient pressure was used to determine the instrument parameters for refinements via GSAS-II [26,27]. All measurements were performed at room temperature.

Bulk magnetization measurements were made in a superconducting quantum interference device (SQUID) magnetometer (magnetic property measurement system, Quantum Design) between 5 and 350 K with the c axis of the sample oriented parallel or perpendicular to the magnetic field. Magnetic measurements under pressure used a Cu-Be piston cell (Almax easyLab Mcell 10) up to 0.7 GPa. The sample was immersed in a pressure-transmitting medium of Fluorinert, and the pressure was determined using the superconducting transition of a Sn manometer inside the pressure cell [28].

Resistivity and magnetoresistance (MR) measurements were performed in a 160 kOe superconducting magnet system (physical property measurement system, Quantum Design) using the four-probe AC transport option ($f = 17$ Hz) with the external magnetic field applied parallel to the c axis of the sample. High-pressure measurements were performed on a monolithic polycrystalline sample (approximately $50 \times 50 \times 10\,\mu m^3$) using an eight-probe *designer* DAC [29–32] with steatite as the pressure-transmitting medium and ruby as the pressure calibrant (see the Appendix for further details). The maximum pressure employed in this paper was 16.2 GPa.

III. RESULTS AND DISCUSSION

Iron-deficient $Fe_{2.75}GeTe_2$ is a weak itinerant ferromagnet that crystallizes into a hexagonal structure with the space group of $P6_3/mmc$. The structure consists of two distinct Fe sites that are tetrahedrally coordinated to Ge and Te atoms and form sheets that are vdW bonded between each unit layer (Fig. 1, inset). The following lattice parameters were obtained from the ambient-pressure room-temperature XRD measurements $a = 3.9555(3)$ and $c = 16.3887(1)$ Å, consistent with the lattice parameters reported by May *et al.* [$a = 3.9421(9)$ and $c = 16.378(5)$ Å] [15]. The magnetic properties at ambient pressure (Fig. 1) show a preferred out-of-plane magnetization along the c axis of the crystal and a T_C of ~155 K, which is close to reports for $Fe_{2.8}GeTe_2$ ($T_C = 154$ K) [15]. The transition temperature is determined via differentiation of the temperature-dependent magnetization curves dM/dT.

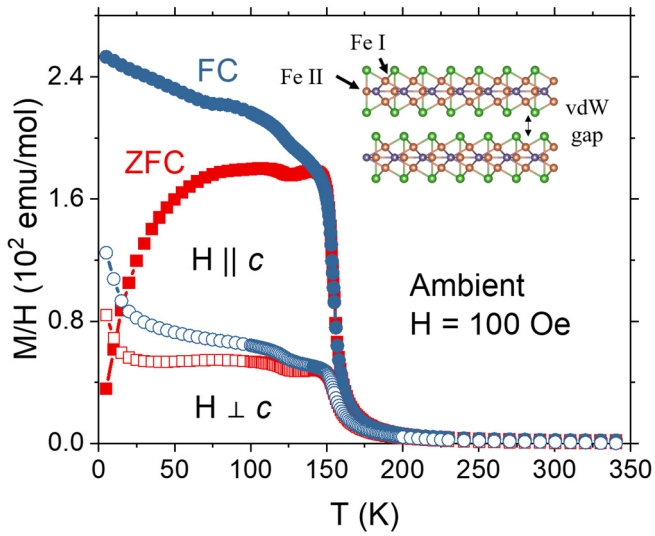

FIG. 1. Ambient pressure temperature-dependent magnetization measurement showing $T_C = 155$ K and easy axis along c. Closed symbols are with the magnetic field along the c axis, and open symbols are with the field on the ab plane. The inset: Ball-and-stick model showing $Fe_{3-x}GeTe_2$ crystal structure from the side view where the green, orange, and purple balls represent Te, Fe, and Ge atoms, respectively.

Chemical doping studies of $Fe_{3-x}GeTe_2$ crystals demonstrated that T_C is correlated with the quantity of Fe vacancies and the degree to which they distort the crystal structure [15]. With increasing Fe vacancies, the structure contracts along the a axis whereas it expands along the c axis, leading to a decrease in T_C to 140 K, whereas fewer Fe vacancies leads to an increase in the T_C [15]. Furthermore, substitution of Fe with either Co or Ni, leads to a gradual suppression in the ferromagnetic ordering due to a transition to a glassy magnetic phase [16,17]. The effect of substitution of Co or Ni on T_C can be viewed as increasing the concentration of Fe vacancies, and, therefore, the evolution of T_C with Co or Ni substitution closely mimics the evolution of T_C with Fe vacancies [15–17]. Although prior work is used as a guide, the application of hydrostatic pressure compresses both crystal axes, potentially leading to different effects on the ordering temperature. The XRD patterns from 0.7(2) to 29.4(4) GPa show a gradual shift in peak position to higher 2θ angles indicative of a smaller unit cell [Appendix Fig. 9(a)]. All the diffraction peaks can be identified, indexed and refined with peaks from the sample $Fe_{2.75}GeTe_2$, an impurity $FeTe_2$, the pressure marker Au, and the gasket (Re). Figures 2(a)–2(d) show monotonic decreases in the lattice parameters, c/a ratio, and volume as functions of pressure with no evidence of a phase transition. The absolute compression of the c axis is more than the a axis across the pressure range of these measurements, which is likely a

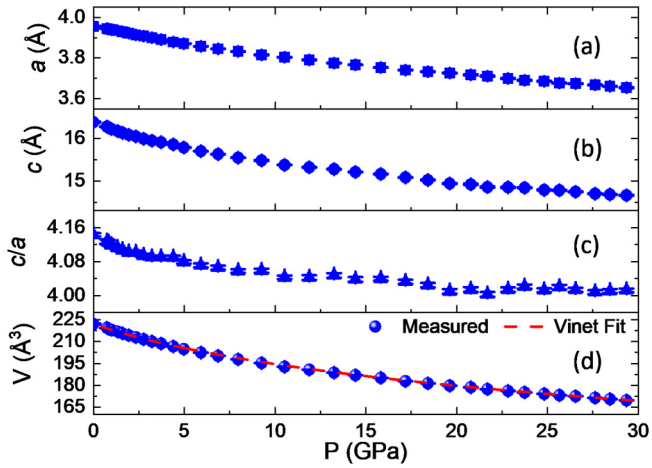

FIG. 2. Room-temperature XRD measurements showing the compression of the unit-cell parameters and volume. There is no indication of a phase transition, and the c axis is compressed about 4% more than the a axis by 30 GPa.

consequence of the weak interlayer vdW interaction (van der Waals gap at ambient pressure 2.95 Å). The pressure versus volume curve in Fig. 2(d) shows a reduction of approximately 25% near 30 GPa. This pressure evolution can be well fit by a Rose-Vinet equation of state with a bulk modulus (K) of 52(8) GPa and pressure derivative (K') of 5.8(1) [33], comparable to other vdW crystals under high pressure, such as WSe_2 [$K = 72(5)$ and $K' = 4.6(5)$] [34]. The detailed Rietveld refinement results is presented in the Appendix [Fig. 9(b)].

A series of isobaric electrical resistance (R_{xx} and R_{xy}) measurements are performed as a function of applied magnetic field to develop an understanding on how compression of the structure affects the material's electronic and magnetic properties. Figure 3(a) is a schematic of a *designer* DAC where the electrical leads are embedded in the diamond anvils [29–32]. The in-plane resistance $R_{xx}(T)$ for a series of pressures is shown in Fig. 3(b) normalized to $R(T = 300\,\mathrm{K})$. The electronic properties change as a function of applied pressure, evolving from a metallic state ($dR/dT > 0$) at ambient pressure to a seemingly nonmetallic state ($dR/dT < 0$) at the highest pressures. Measurements on stoichiometric Fe_3GeTe_2 (bulk $T_C = 220\,\mathrm{K}$) denote a "kink" in the $\rho_{xx}(T)$ curve that represents the transition from a ferromagnetic to paramagnetic phase [21]. This kink is most easily quantified with the temperature derivative of resistivity $d\rho_{xx}/dT$, but this feature becomes smeared out at pressures above 13.4 GPa ($T_C \approx 120\,\mathrm{K}$) [21] likely due to deviatoric stress in the sample compartment at these pressures. A similar broadening of the dR_{xx}/dT curve for pressures above 4.1 GPa makes it challenging to determine the T_C using this method. Although there is a clear trend indicating the Curie temperature decreases with increasing pressure, the broadening of the transition with increasing pressure limits a precise determination of T_C, particularly at higher pressures.

Figure 4 presents both the symmetric (R_{xx}) and antisymmetric components (R_{xy}) of the MR curves as functions of pressure and temperature (see the Appendix for a detailed discussion). The isothermal $R_{xx}(H)$ data have been normalized using the following expression:

$$\mathrm{MR}\ (\%) = \frac{\Delta R}{R} = \frac{R - R_0}{R_0} \times 100\%, \tag{1}$$

where R is the resistance at a given magnetic field and R_0 is the resistance at zero field. The symmetric MR curves show negative MR at low pressures—which is common in ferromagnetic compounds because of the suppression of spin scattering via a magnetic field [12,35,36] and an increase in magnitude of the MR up to 11 GPa followed by a gradual decrease in magnitude at higher pressures [Fig. 4(a)]. The MR transitions from sublinear with H to linear as temperatures increase and no saturation behavior is observed [Fig. 4(b)].

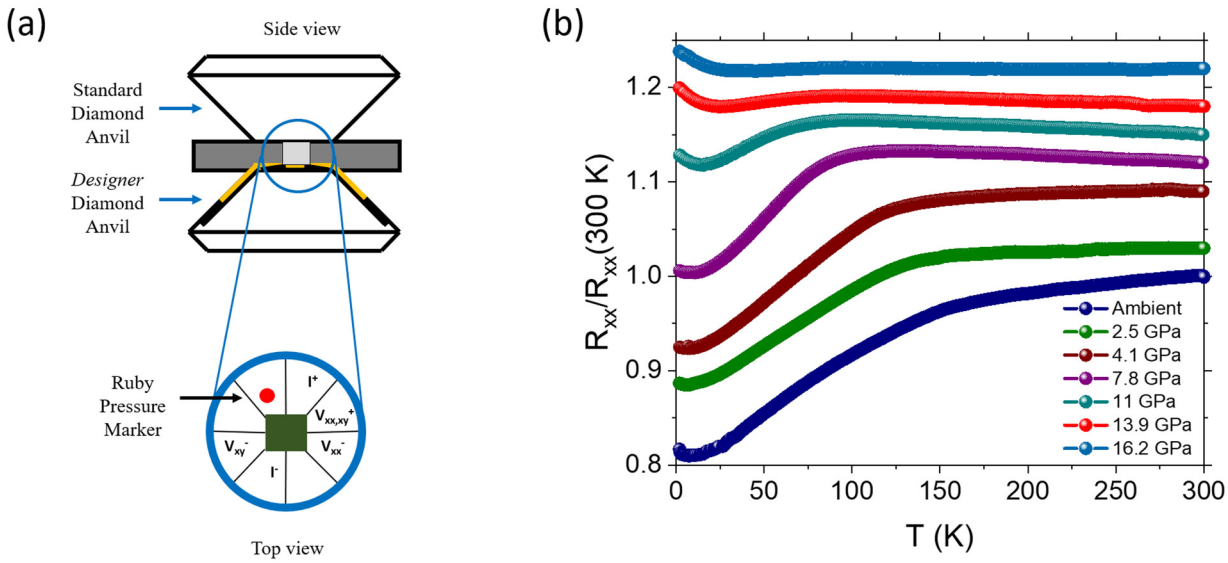

FIG. 3. Resistance of $Fe_{3-x}GeTe_2$ measured at a series of increasing pressures. (a) Schematic of the designer DAC used for electrical measurements. (b) Normalized resistance measurements for cross comparison (offset for clarity). The change in slope is an indication of the Curie temperature in each trace. With increasing pressure, the paramagnetic region changes from metallic to nonmetallic.

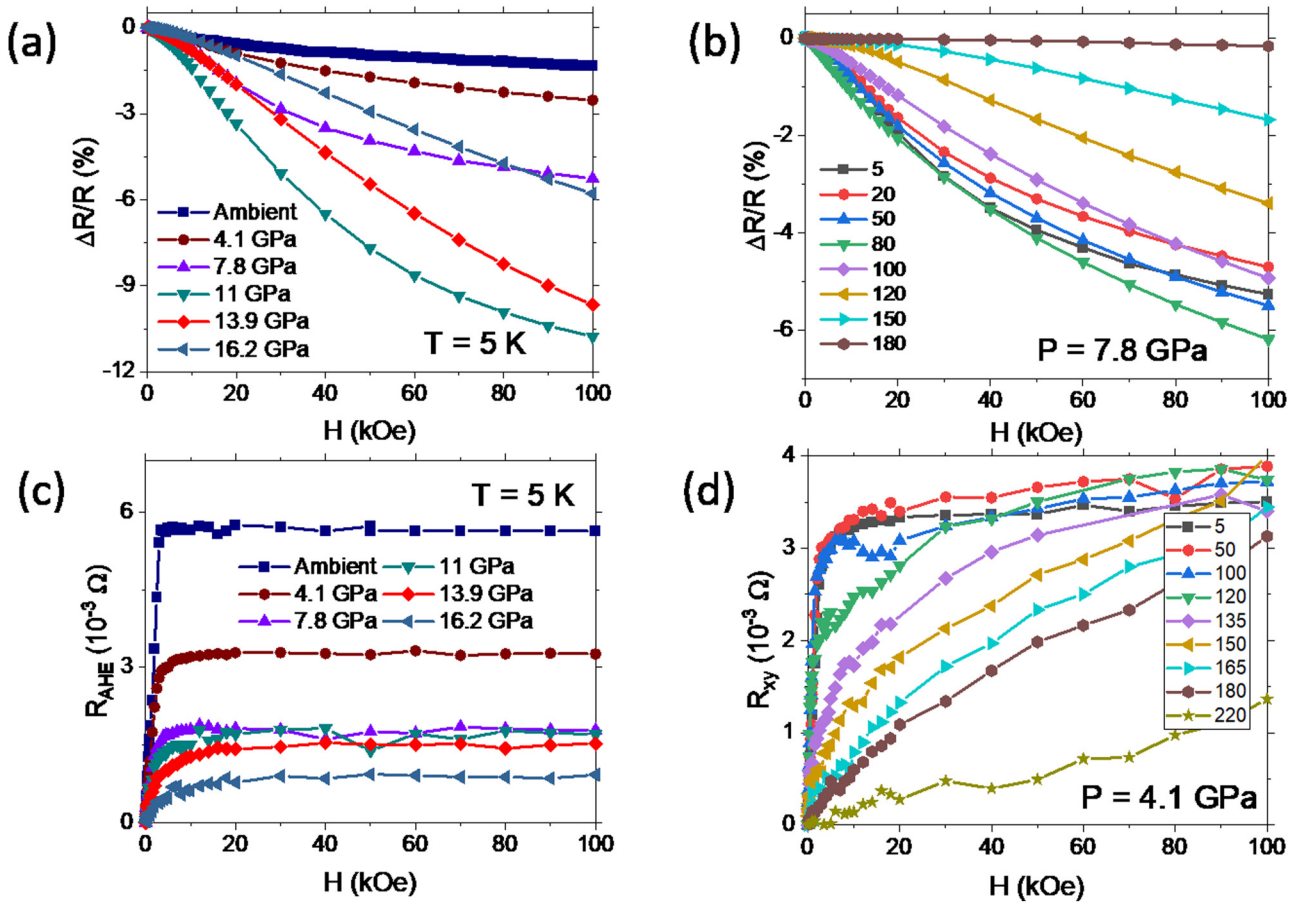

FIG. 4. MR measurements. (a) Negative MR at 5 K for several pressures showing the greatest relative change at 11 GPa. (b) Negative MR at 7.8 GPa showing changes in shape (linear versus sublinear) as a function of temperature due to magnon scattering. $R_{xy}(H)$ scans showing changes in magnitude as a function of temperature and pressure where (c) the AHE component shows suppression of magnitude from compression of the $Fe_{2.75}GeTe_2$ crystal and (d) shows the raw data as a function of temperature at 4.1 GPa where the signal is dominated by the linear ordinary Hall component above T_C and a low-field saturation below T_C.

The transition to the weaker nonsaturating linear region is consistent with the presence of magnon scattering at elevated temperatures near T_C [36–39], and, with increasing pressure, this transition temperature decreases (not shown).

Additional insight is gleaned from the $R_{xy}(H)$ data. For ferromagnetic conductors, the $R_{xy}(H)$ has two components contributing to the signal as shown in the expression,

$$R_{xy} = R_H H + R_{AHE} = R_H H + R_S M, \tag{2}$$

where $R_H H$ represents the ordinary Hall effect and R_{AHE}, an additional nonlinear ferromagnetic contribution known as the anomalous Hall effect (AHE), which is directly proportional to R_S, a scattering coefficient, and $M(H)$, the magnetization [12,40]. At 5 K, there is a distinct linear region at high fields due to saturation of the magnetization. To isolate the AHE contribution, we fit the linear region where the $R_{xy}(H)$ shows only linear behavior and above the ambient pressure magnetic saturation [$\sim$5 kOe, Appendix Fig. 8(b)], spanning from 5 to 100 kOe [31]. This linear component is then subtracted from the measured signal to yield the AHE component. This is shown in Fig. 4(c) as a function of pressure and temperature, respectively. With increasing pressure, the overall saturation value of the R_{AHE} signal decreases as pressure increases, consistent with the observations of Wang *et al.* [21] due to the decrease in T_C and the gradual suppression of the Fe magnetic moment. For the temperature dependence, we plot the total $R_{xy}(H)$ including the AHE and ordinary Hall contributions [Fig. 4(d)], which suggests a change from a ferromagnetic to a paramagnetic state. At temperatures of 135 K and above (at 4.1 GPa), the change in slope from a dominating nonlinear AHE contribution to a dominating linear contribution of R_H is a signature of T_C. T_C is determined quantitatively by first defining S as the slope of $R_{xy}(H)$ from 0 to 1 kOe and plotting S as a function of temperature for various pressures [Fig. 5(a)]. The raw data are shown in the Appendix (Fig. 11). Since the AHE component of R_{xy} is proportional to magnetization M, the slope S is proportional to the susceptibility, $\chi = dM/dH$, plus an offset from the ordinary Hall effect. Accordingly, the S versus T curves [Fig. 5(a)] have similar shapes as the M versus T curves from magnetic measurements (Fig. 1) where the ferromagnetic-to-paramagnetic transition with increasing temperature is identified by a strong reduction in signal (S or M) at T_C.

The derivative of S (i.e., dS/dT) is taken to determine T_C and is shown in Fig. 5(b), designated by arrows and shows a decreasing trend with higher pressure. Furthermore, there is no signature of a transition temperature in the dS/dT data at 16.2 GPa, which suggests that the ferromagnetism may be

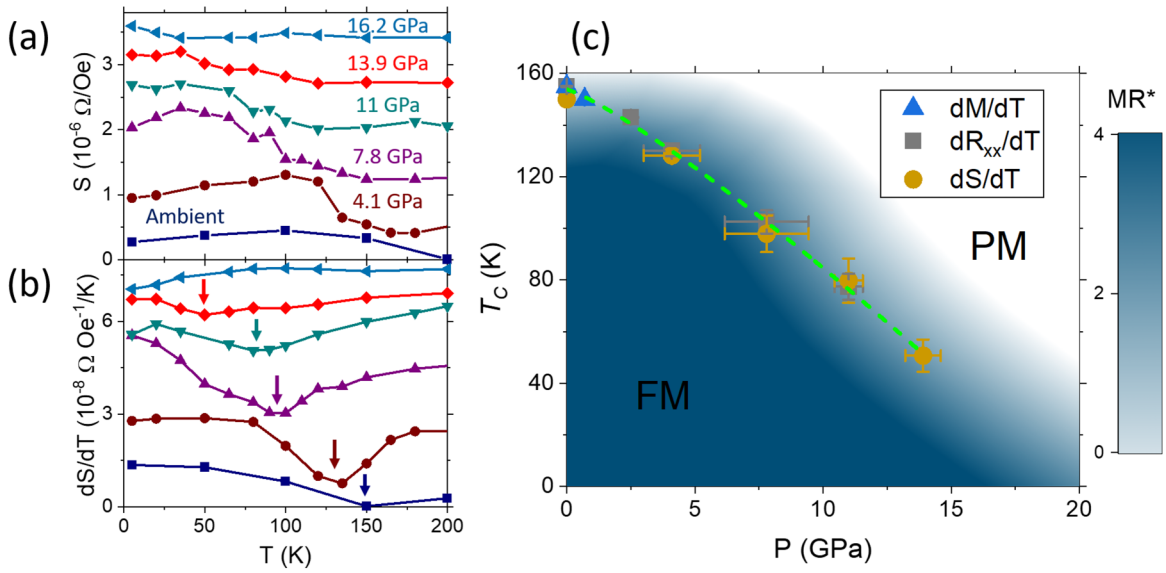

FIG. 5. (a)-(b) T_C determined from AHE data. S is defined as the initial slope of the $R_{xy}(H < 1\ \text{kOe})$ curve. The derivative shows a dip near/at T_C where arrows indicate the local minimum of a Lorentzian fit (this fitting is also used to determine error bar for T_C). The plotted data are offset for clarity. There is no measurable transition temperature above 13.9 GPa, therefore, an arrow denoting T_C at 16.2 GPa is not shown in (b). (c) P-T phase diagram showing T_C determined by these approaches. The dashed line is a parabolic fit of the data to 13.9 GPa for a guide to the eye. The T_C shows a monotonic decrease at a decay rate of 7.4 K/GPa. The contour regions show $\text{MR}^* = d^2\text{MR}/dH^2$ at $H = 60$ kOe (in units of $10^{-12}\ \Omega/\text{Oe}^2$) where the change from zero is consistent with indications of ferromagnetic ordering. Pressure error bars are determined via a difference of pressure before and after temperature cycles, and details are discussed in the Appendix.

suppressed or that pressure smears the transition until it is undistinguishable. A combination of the dM/dT, dR_{xx}/dT, and dS/dT curves are used to plot the T_C for pressures above ambient conditions (see Table I for quantified T_C values from different methods) and are plotted on a temperature-pressure phase diagram. This pressure-dependent reduction of the T_C is shown in Fig. 5(c) with different methods of determination and a parabolic extrapolation to higher pressures showing a monotonic decrease at a decay rate of ∼7.4 K/GPa. A contour map designating the ferromagnetic and paramagnetic regions of the phase diagram using the second derivative of the local negative MR curvature at magnetic saturation [as seen in Fig. 4(b)] is denoted as MR*. The represented data are fixed at a field of 60 kOe and, for the same trend, is present for any large field above saturation. Note that the MR* map of the phase diagram shows possible magnetic ordering at $P > 14$ GPa, closely following the parabolic fitting but is not direct evidence of ferromagnetic ordering [41]. For pressures below 2 GPa, bulk magnetization measurements confirm the downward trend in ordering temperature (Appendix Fig. 12). The absence of evidence of a T_C beyond 13.9 GPa is consistent with Ref. [21] where a transition temperature could not be distinguished for pressures higher than 13.4 GPa. It should be noted that the application of pressure to this Fe-deficient sample lowers the absolute temperature where the ferromagnetic transition remains detectable as compared to the stoichiometric sample in Ref. [21].

Figures 6(a) and 6(b) show the T_C as a function of the unit-cell parameters compared to the results of pressurized stochiometric Fe_3GeTe_2 [21] and chemical doped $Fe_{3-x}GeTe_2$ [15] which the T_C drops from ∼200 K close to 50 K as a function of compressed lattice parameters. In Ref. [15], the reduced T_C correlates with the reduction of a, expansion of c, an increased Fe(I)-Fe(I) bond distance, and a decreased Fe(I)-Fe(II) bond distance. In the present paper, pressure causes both a and c to decrease with corresponding reductions in both the Fe(I)-Fe(I) and the Fe(I)-Fe(II) atomic distances. This is accompanied by a reduced T_C and could be evidence of spin-lattice coupling from pressure-induced compression of the crystal. Figure 6

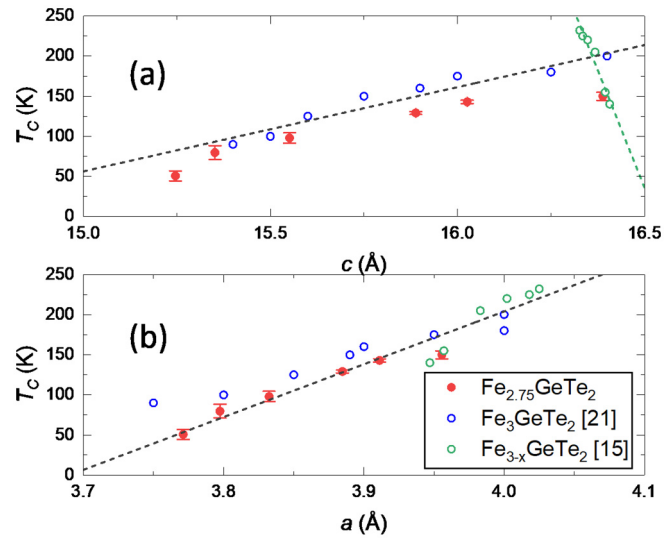

FIG. 6. (a)-(b) T_C as a function of unit-cell parameters. The red and blue data are the results of pressure measurements whereas the green circles show a variation in x from 0 to 0.3 for $Fe_{3-x}GeTe_2$. The variation in the a lattice parameter is consistent for all three sets of measurements whereas the c axis parameter is not.

shows the a axis is very closely correlated with the decrease in T_C with the link being less clear for the c axis. The T_C decreases with decreasing a axis in all three cases, and a linear extrapolation shows a reduction close to 5 K at 3.7 Å whereas for the c axis, it deviates with opposite slope while applying chemical pressure. This provides evidence that intralayer exchange coupling plays a larger role in the T_C reduction than the interlayer exchange coupling.

Another possibility is that because $Fe_{2.75}GeTe_2$ is a weak itinerant ferromagnet, the $3d$-electron bandwidth of the spin density of states (spin-DOS) near the Fermi level should broaden as volume decreases which will lead to a corresponding decrease in the Stoner factor and thereby reduce the Curie temperature based on the Stoner criterion for magnetic ordering [42,43]. This should lead to a reduction in the splitting of the spin-DOS bands, thus, decreasing the magnetic moment eventually resulting in a nonmagnetic state. To confirm this, we combine our bulk magnetization and AHE data at 5 K under pressure and use this to calculate a Rhodes-Wohlfarth ratio (RWR) [44,45]. RWR is defined as p_c/p_s with p_c obtained from the effective moment calculated from the Curie-Weiss susceptibility,

$$p_c(p_c + 2) = p_{\text{eff}}^2, \tag{3}$$

and p_s is the saturation moment obtained at low temperatures. RWR is 1 for localized systems and is larger in an itinerant (delocalized) system. Here, we take p_s as the magnetization saturation obtained at 5 K and 50 kOe, so the calculated RWR values are ~4.0. The RWR shows that the system becomes more delocalized with pressure, which is consistent with chemical doping studies on $Fe_{3-x}GeTe_2$ [15,46] and supports the explanation of reduced T_C in terms of the Stoner criterion. Thus, the reduction of the magnetic moment (and, subsequently, T_C) is caused by the diminished $3d$-electron correlations likely due to the shortening of the Fe(I)-Fe(II) distance from increasing pressure. A combination of a spin-wave or x-ray scattering experiment under pressure and theoretical support will further address the itinerant nature of this system and is needed to confirm this observation.

IV. CONCLUSIONS

This paper is a systematic study of the effect of pressure on the resistance and MR of Fe-deficient $Fe_{2.75}GeTe_2$. In the absence of applied pressure, Fe-deficient $Fe_{2.75}GeTe_2$ shows negative MR and metallic behavior, and the magnetic easy axis is along the c direction. T_C decreases linearly from 155 to ~50 K with increasing the pressure to 13.9 GPa. Although there is evidence that ferromagnetic ordering may exist above this pressure, confirmation requires a low-temperature measurement of the crystal structure and a direct measurement of the magnetization under pressure. The electronic transport implies a transition from a metallic to a nonmetallic state with increasing pressure up to 16.2 GPa. $R_{xy}(H)$ measurements are used to quantify the evolution of T_C up to nearly 14 GPa and are used in combination with other methods to generate a magnetic P-T phase diagram. The effect of pressure on $Fe_{2.75}GeTe_2$ illustrates the value of pressure as a tool to better understand the underlying mechanisms for magnetic ordering in vdW systems.

ACKNOWLEDGMENTS

This work was performed under the auspices of the U.S. Department of Energy (DOE) by LLNL under Contract No. DE-AC52-07NA27344. Part of the funding was provided through the LLNL Lawrence Graduate Scholar Program. D.J.O. acknowledges support from the GEM National Consortium Ph.D. Fellowship. Portions of this work were performed at HPCAT (Sector 16), Advanced Photon Source, Argonne National Laboratory (ANL). HPCAT operations are supported by DOE-NNSA's Office of Experimental Sciences. The APS is a U.S. DOE of Science User Facility operated for the DOE Office of Science by ANL under Contract No. DE-AC02-06CH11357. D.W., J.E.G., and R.K.K. acknowledge support from the Center for Emergent Materials, an NSF MRSEC under Grant No. DMR-1420451. Z.E.B. and R.J.Z. acknowledge support from NSF Grant No. DMR-1609855. We thank J. Beckham, J. R. I. Lee (LLNL), and C. Park (HPCAT) for technical assistance. D.J.O. was supported by NRC/NRL while finalizing the paper.

APPENDIX

The elemental composition of the sample was characterized by RBS with a 2-MeV ^{4}He beam. Rutherford backscattering spectrometry (RBS) is a nondestructive method based on high-energy ion scattering, providing depth-resolved information about the elemental composition of near-surface layers [47] (see Fig. 7). For RBS, the He ion beam was incident normal to the sample surface and backscattered into a detector located at 165° from the incident beam. The analysis of RBS spectra was performed with the RUMP code [48].

Phase identification and magnetic properties in ambient conditions were determined using XRD (Cu $K\alpha$, Bruker) and magnetometry. Figure 8(a) shows the ambient XRD pattern of the $Fe_{2.75}GeTe_2$ polycrystalline sample with an observation

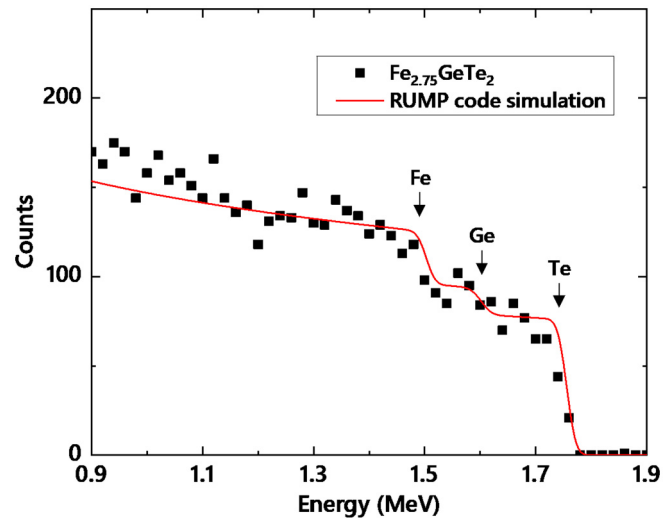

FIG. 7. Rutherford backscattering spectra from $Fe_{2.75}GeTe_2$ sample. Symbols are experimental points, whereas solid lines are results of RUMP-code simulations. For clarity, only every tenth experimental point is depicted. Surface edges of Fe, Ge, and Te are marked by arrows.

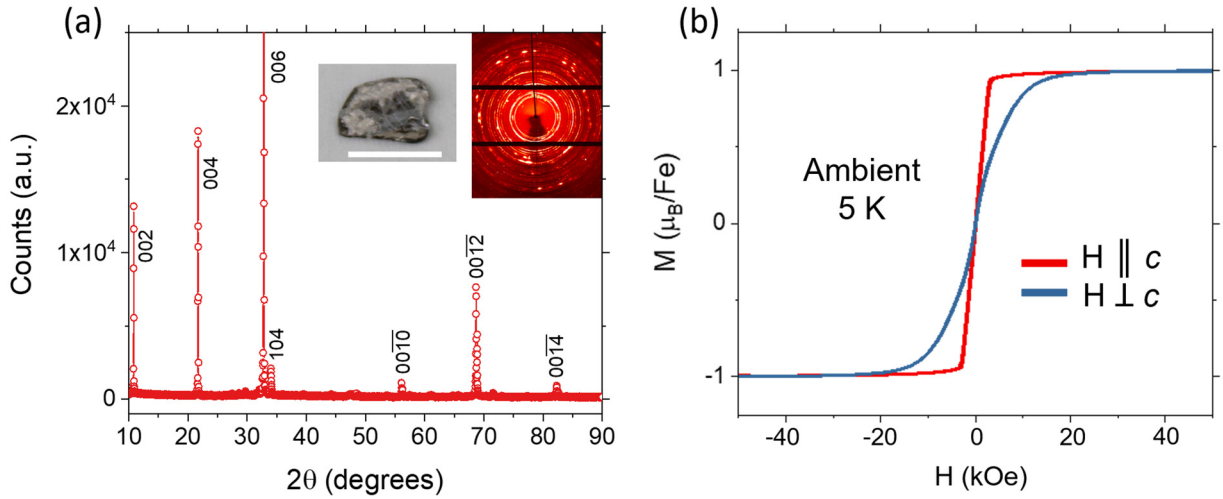

FIG. 8. Ambient pressure measurements of $Fe_{2.75}GeTe_2$ with (a) showing XRD with a preferred texture along the c axis. The inset: Photograph of $Fe_{2.75}GeTe_2$ sample used in measurements (left) and 2D diffraction image showing polycrystallinity in the sample (right). Scale bar is 5 mm. Black lines are from the image plate. (b) $M(H)$ measurements at 5 K showing magnetic anisotropy along the c axis of the crystal.

of strong diffraction peaks along the (0 0 $2l$), indicating a high c-axis orientation of the crystal. The indexing and refinement of the peaks aligns with previous reports [15]. The insets show a laboratory photograph (scale bar is 5 mm) and a 2D diffraction image showing the crystallinity of the sample. Figure 8(b) depicts the $M(H)$ loops at 5 K where the magnetization prefers to lie along the c axis and saturates at approximately 5 kOe.

Angle-dispersive x-ray diffraction measurements under pressure were performed at room temperature using beamline 16 BM-D (HPCAT) of the Advanced Photon Source at Argonne National Laboratory. A gas membrane-driven DAC composed of two 500-μm diamond anvils was used to generate pressures up to 29.4(4) GPa [22]. A rhenium gasket was preindented to a thickness of 60 μm, and a 180-μm hole was drilled using a wire electric discharge machine in the center of the gasket to serve as a sample chamber. The sample was ground into a powder with a mortar and pestle under inert glovebox conditions. The powders were then loaded into the DAC sample chamber and mixed with Au powder, which served as an x-ray pressure calibrant, and a ruby sphere was used for initial pressure calibration. The Au bulk modulus (K) and Au pressure derivative (K') are 167 GPa and 6, respectively [23]. Neon gas was used as the pressure-transmitting medium. Ne is essentially hydrostatic up to ~15 GPa and at pressures above that the uniaxial stress remains low [49]. Incident x-rays with a monochromated energy of 30 keV ($\lambda = 0.413\,28$ Å) were microfocused to a 12×5-μm^2 spot. X-ray diffraction measurements were performed in a transmission geometry, and a MAR345 image plate was used as the detector with 120-s exposures at each pressure. The detector was calibrated using CeO_2. The resulting 2D diffraction patterns from the detector

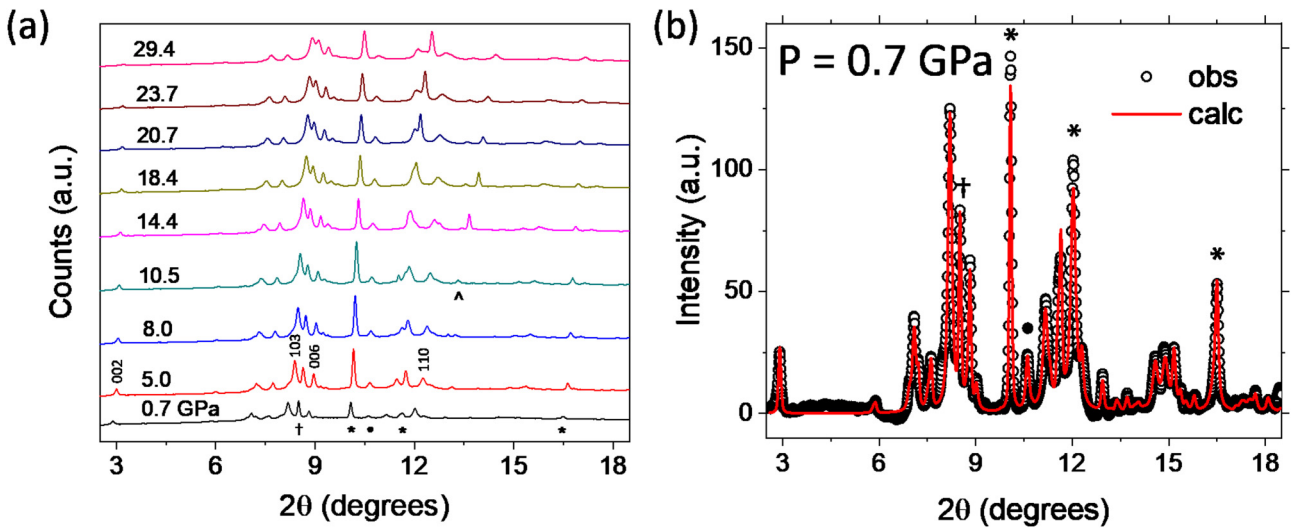

FIG. 9. (a) XRD plotted as a function of pressure showing compression of the unit cell with higher 2θ angles. (b) Rietvield refinement of powdered $Fe_{2.75}GeTe_2$ at 0.7 GPa. †, *, and • are $FeTe_2$, Au pressure marker, and Re gasket, respectively. All other unlabeled indexed peaks are the sample. The ^ symbol is indicating solidification of the neon gas at higher pressure.

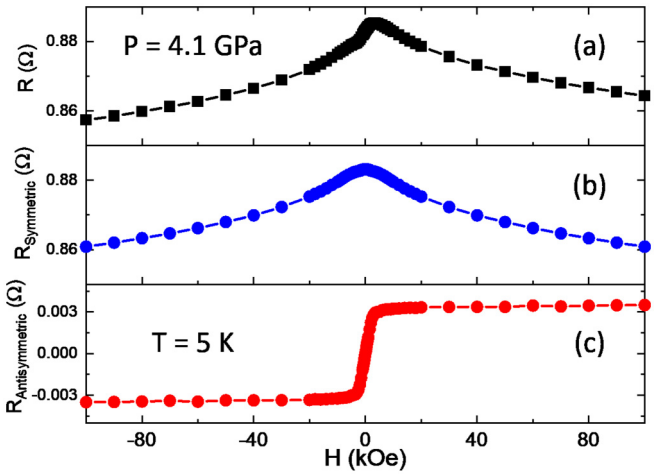

FIG. 10. Magnetoresistance measurements at a select pressure of 4.1 GPa and select temperature of 5 K. (a) Raw electrical resistance data as a function of applied magnetic field showing nonsymmetric MR about the zero field. (b) Symmetrized and (c) antisymmetrized data showing both R_{xx} and R_{xy} contributions in the raw $R(H)$ measurement.

were integrated to obtain conventional one-dimensional powder patterns using the program DIOPTAS [25]. Refinements of the lattice parameters were performed using GSAS-II [26,27] and are shown in Fig. 9 at 0.7(2) GPa. These samples contain a Fe-deficient phase of nonmagnetic $FeTe_2$ (orthorhombic, *Pnnm*), which is considered in the XRD refinement analysis but excluded from the main text of the paper. Ne is observed in Fig. 9(a) at pressures above ∼4.6 GPa, which is consistent with Ref. [49].

Electrical transport studies under pressure were performed on a small polycrystal of $Fe_{2.75}GeTe_2$ using an eight-probe *designer* DAC [29,30] with steatite as a pressure-transmitting medium and ruby as the pressure calibrant. The gasket was made of the nonmagnetic alloy MP35N, preindented to a thickness of 40 μm, and a 100-μm diameter hole was drilled in the center of the gasket using a wire electric discharge machine. The crystal was cleaved to an ∼10-μm thickness with a cross-sectional area of $\sim 50 \times 50\,\mu m^2$. Electrical contact to the sample was made via the exposed tips of the tungsten microprobes at the culet of the diamond anvil. To ensure good contact between the sample and the microprobes, steatite was initially precompressed into the gasket hole, and then the sample was placed on top of the steatite so that when the DAC was closed, the steatite pressed the sample against the leads. The pressure was determined by a single ruby, so no measurements of gradients were possible. However, based on previous measurements in this *designer* DAC, gradients on the order of 5% are expected [32], which is consistent with values reported by Klotz *et al.* [49]. Pressure was determined at room temperature by averaging the shift of the R_1 ruby fluorescence peak before and after temperature cycles. The uncertainty was determined by the difference of P_{max} and P_{min}, where P_{max} and P_{min} are the pressures before and after temperature cycles. If the difference after temperature cycles is larger than 5%, then this spread is chosen as the error bar. Electrical transport measurements under pressure were performed as a function of temperature and magnetic field using the AC transport option in a Quantum Design physical property measurement system. MR measurements were taken at each pressure using an excitation current of 0.316 mA at a frequency of 17 Hz.

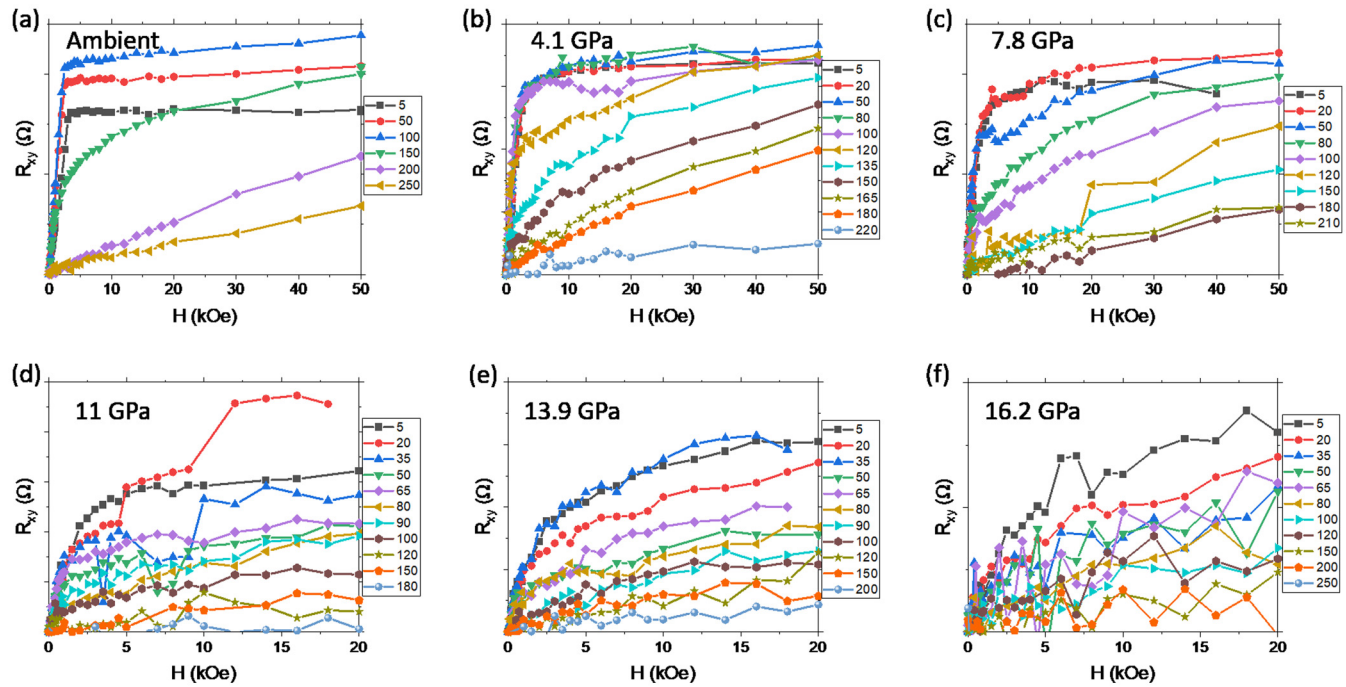

FIG. 11. (a)–(f) Antisymmetrized $R_{xy}(H)$ measurements as a function of temperature at a given pressure. R_{xy} curve transitions from a nonlinear saturating curve indicative of ferromagnetism below T_C to a linear nonsaturating curve above T_C.

TABLE I. Determination of magnetic ordering temperature at select pressures (n/a represents not available).

Pressure (GPa)	$T_{C,1}$ (K)	$T_{C,2}$ (K)
2.5	143	n/a
4.1	130	128.2
7.8	102.5	97.8
11	77.4	79.7
13.9	n/a	50.6
16.2	n/a	n/a

The magnetoresistance $R_{xx}(H)$ where the current is passed along the *ab* plane of the sample and the magnetic field is along the *c* axis of the sample is symmetrized by sweeping the magnetic field over both the negative and the positive field ranges. The sum was then calculated between the resistances over the positive and negative field regions and divided by two to extract the resistance solely due to the MR. In the same manner, the Hall resistance $R_{xy}(H)$ where the current is passed perpendicular to the measured voltage and magnetic field is antisymmetrized by taking the difference of the resistances over the negative and positive magnetic field regions and dividing by two. This procedure is displayed in the graphs in Fig. 10 where the raw data show both R_{xx} and R_{xy} signals due to the irregular shape of the sample. For clarity in the main text, the positive magnetic-field values are only displayed. Temperature-dependent $R_{xy}(H)$ curves are shown in Fig. 11 denoting a sublinear saturating (below T_C) curve transition to a linear nonsaturating curve (above T_C).

At ambient pressure, the T_C is determined via the differentiation of the M(T) curve in Fig. 1 of the main text. For pressures from 2.5 to 11 GPa, the T_C of pressurized $Fe_{2.75}GeTe_2$ is quantified by taking dR_{xx}/dT (labeled $T_{C,1}$). For pressures from 4.1 to 13.9 GPa, the T_C is determined via the dS/dT curve shown in Fig. 5(b) of the main text (labeled $T_{C,2}$ below). The quantified T_C is shown in Table I below.

To perform hydrostatic pressures up to 0.7 GPa in a SQUID magnetometer, piston pressure cells were used. The Quantum Design SQUID magnetometer is equipped with a rod attachment for these types of pressure cells. A $Fe_{2.75}GeTe_2$ crystal was placed inside a small cylindrical polytetrafluoroethylene cap along with a Sn manometer (as a pressure calibrant) and a pressure-transmitting medium of Fluorinert. The Fluorinert remains hydrostatic up to the maximum pressure in these experiments, and the deviatoric stress is known to be very low for pressures up to and above 0.7 GPa, at least, until ~ 7 GPa [49]. This was then placed in the middle of the Cu-Be pressure cell and held in place by extrusion disks and ceramic pistons. Samples were externally pressurized via a piston hydraulic press (Mpress Mk2). After each pressurization, samples were attached to the sample rod via threading and loaded into the chamber. The pressure cell was then cooled down slowly below the transition temperature of the superconducting Sn manometer and positioned accordingly. $M(T)$ measurements were performed at each pressure, and these are displayed in the inset of Fig. 12. The differentiation of the magnetization curves dM/dT shows a downward trend in the T_C. The T_C is plotted as a function of pressure showing approximately a 6 K decrease.

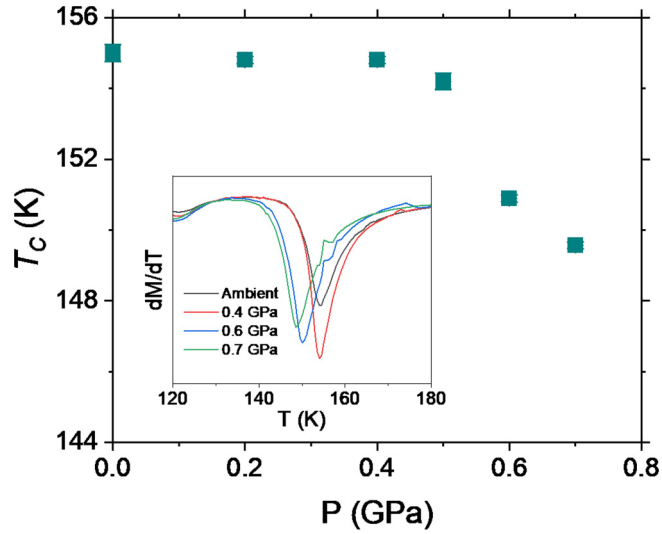

FIG. 12. Pressure measurements using the magnetometer showing a drop in T_C with pressures up to 0.7 GPa.

[1] C. Gong, L. Li, Z. L. Li, H. W. Ji, A. Stern, Y. Xia, T. Cao, W. Bao, C. Z. Wang, Y. A. Wang *et al.*, Nature (London) **546**, 265 (2017).

[2] B. Huang, G. Clark, E. Navarro-Moratalla, D. R. Klein, R. Cheng, K. L. Seyler, D. Zhong, E. Schmidgall, M. A. McGuire, D. H. Cobden *et al.*, Nature (London) **546**, 270 (2017).

[3] Z. Wang, I. Gutierrez-Lezama, N. Ubrig, M. Kroner, M. Gibertini, T. Taniguchi, K. Watanabe, A. Imamoglu, E. Giannini, and A. F. Morpurgo, Nat. Commun. **9**, 8, 2516 (2018).

[4] B. Huang, G. Clark, D. R. Klein, D. MacNeill, E. Navarro-Moratalla, K. L. Seyler, N. Wilson, M. A. McGuire, D. H. Cobden, D. Xiao *et al.*, Nat. Nanotechnol. **13**, 544 (2018).

[5] E. S. Morell, A. Leon, R. H. Miwa, and P. Vargas, 2D Mater. **6**, 025020 (2019).

[6] D. J. O'Hara, T. C. Zhu, A. H. Trout, A. S. Ahmed, Y. K. Luo, C. H. Lee, M. R. Brenner, S. Rajan, J. A. Gupta, D. W. McComb *et al.*, Nano Lett. **18**, 3125 (2018).

[7] M. Bonilla, S. Kolekar, Y. J. Ma, H. C. Diaz, V. Kalappattil, R. Das, T. Eggers, H. R. Gutierrez, M. H. Phan, and M. Batzill, Nat. Nanotechnol. **13**, 289 (2018).

[8] D. Weber, A. H. Trout, D. W. McComb, and J. E. Goldberger, Nano Lett. **19**, 5031 (2019).

[9] Z. Y. Fei, B. Huang, P. Malinowski, W. B. Wang, T. C. Song, J. Sanchez, W. Yao, D. Xiao, X. Y. Zhu, A. F. May *et al.*, Nat. Mater. **17**, 778 (2018).

[10] C. Tan, J. Lee, S. G. Jung, T. Park, S. Albarakati, J. Partridge, M. R. Field, D. G. McCulloch, L. Wang, and C. Lee, Nat. Commun. **9**, 1554 (2018).

[11] G. D. Nguyen, J. Lee, T. Berlijn, Q. Zou, S. M. Hus, J. Park, Z. Gai, C. Lee, and A. P. Li, Phys. Rev. B **97**, 014425 (2018).
[12] Y. H. Wang, C. Xian, J. Wang, B. J. Liu, L. S. Ling, L. Zhang, L. Cao, Z. Qu, and Y. M. Xiong, Phys. Rev. B **96**, 134428 (2017).
[13] S. S. Liu, X. Yuan, Y. C. Zhou, Y. Sheng, C. Huang, E. Z. Zhang, J. W. Ling, Y. W. Liu, W. Y. Wang, C. Zhang *et al.*, npj 2D Mater. Appl. **1**, 30 (2017).
[14] J. Y. Yi, H. L. Zhuang, Q. Zou, Z. M. Wu, G. X. Cao, S. W. Tang, S. A. Calder, P. R. C. Kent, D. Mandrus, and Z. Gai, 2D Mater. **4**, 011005 (2017).
[15] A. F. May, S. Calder, C. Cantoni, H. B. Cao, and M. A. McGuire, Phys. Rev. B **93**, 014411 (2016).
[16] G. Drachuck, Z. Salman, M. W. Masters, V. Taufour, T. N. Lamichhane, Q. Lin, W. E. Straszheim, S. L. Bud'Ko, and P. C. Canfield, Phys. Rev. B **98**, 144434 (2018).
[17] C. K. Tian, C. Wang, W. Ji, J. C. Wang, T. L. Xia, L. Wang, J. J. Liu, H. X. Zhang, and P. Cheng, Phys. Rev. B **99**, 184428 (2019).
[18] H. Yoshida, J. Chiba, T. Kaneko, Y. Fujimori, and S. Abe, Physica B **237**, 525 (1997).
[19] S. Mondal, M. Kannan, M. Das, L. Govindaraj, R. Singha, B. Satpati, S. Arumugam, and P. Mandal, Phys. Rev. B **99**, 180407(R) (2019).
[20] Z. Lin, M. Lohmann, Z. A. Ali, C. Tang, J. Li, W. Xing, J. Zhong, S. Jia, W. Han, S. Coh, W. Beyermann, and J. Shi, Phys. Rev. Materials **2**, 051004 (2018).
[21] X. Wang, Z. Li, M. Zhang, T. Hou, J. Zhao, L. Li, A. Rahman, Z. Xu, J. Gong, Z. Chi, R. Dai, Z. Wang, Z. Qiao, and Z. Zhang, Phys. Rev. B **100**, 014407 (2019).
[22] Z. Jenei, H. Cynn, K. Visbeck, and W. J. Evans, Rev. Sci. Instrum. **84**, 095114 (2013).
[23] Y. W. Fei, A. Ricolleau, M. Frank, K. Mibe, G. Y. Shen, and V. Prakapenka, Proc. Natl. Acad. Sci. USA **104**, 9182 (2007).
[24] A. Dewaele, M. Torrent, P. Loubeyre, and M. Mezouar, Phys. Rev. B **78**, 104102 (2008).
[25] C. Prescher and V. B. Prakapenka, High Pressure Res. **35**, 223 (2015).
[26] B. H. Toby and R. B. Von Dreele, J. Appl. Crystallogr. **46**, 544 (2013).
[27] B. H. Toby, J. Appl. Crystallogr. **34**, 210 (2001).
[28] A. Eiling and J. S. Schilling, J. Phys. F: Met. Phys. **11**, 623 (1981).
[29] S. T. Weir, J. Akella, C. Aracne-Ruddle, Y. K. Vohra, and S. A. Catledge, Appl. Phys. Lett. **77**, 3400 (2000).
[30] D. D. Jackson, J. R. Jeffries, W. Qiu, J. D. Griffith, S. McCall, C. Aracne, M. Fluss, M. B. Maple, S. T. Weir, and Y. K. Vohra, Phys. Rev. B **74**, 174401 (2006).
[31] R. L. Stillwell, J. R. Jeffries, S. K. McCall, J. R. I. Lee, S. T. Weir, and Y. K. Vohra, Phys. Rev. B **92**, 174421 (2015).
[32] J. R. Jeffries, R. L. Stillwell, S. T. Weir, Y. K. Vohra, and N. P. Butch, Phys. Rev. B **93**, 184406 (2016).
[33] P. Vinet, J. R. Smith, J. Ferrante, and J. H. Rose, Phys. Rev. B **35**, 1945 (1987).
[34] X. F. Wang, X. L. Chen, Y. H. Zhou, C. Y. Park, C. An, Y. Zhou, R. R. Zhang, C. C. Gu, W. G. Yang, and Z. R. Yang, Sci. Rep. **7**, 46694 (2017).
[35] R. von Helmolt, J. Wecker, B. Holzapfel, L. Schultz, and K. Samwer, Phys. Rev. Lett. **71**, 2331 (1993).
[36] J. G. Checkelsky, M. Lee, E. Morosan, R. J. Cava, and N. P. Ong, Phys. Rev. B **77**, 014433 (2008).
[37] W. Gil, D. Görlitz, M. Horisberger, and J. Kötzler, Phys. Rev. B **72**, 134401 (2005).
[38] B. Raquet, M. Viret, J. M. Broto, E. Sondergard, O. Cespedes, and R. Mamy, J. Appl. Phys. **91**, 8129 (2002).
[39] B. Raquet, M. Viret, E. Sondergard, O. Cespedes, and R. Mamy, Phys. Rev. B **66**, 024433 (2002).
[40] Y. Liu, E. Stavitski, K. Attenkofer, and C. Petrovic, Phys. Rev. B **97**, 165415 (2018).
[41] V. Taufour, D. Aoki, G. Knebel, and J. Flouquet, Phys. Rev. Lett. **105**, 217201 (2010).
[42] V. Iota, J. H. P. Klepeis, C. S. Yoo, J. Lang, D. Haskel, and G. Srajer, Appl. Phys. Lett. **90**, 042505 (2007).
[43] Z. Y. Zeng, C. E. Hu, X. R. Chen, L. C. Cai, and F. Q. Jing, J. Phys.: Condens. Matter **20**, 425217 (2008).
[44] E. P. Wohlfarth, J. Magn. Magn. Mater. **7**, 113 (1978).
[45] T. Moriya, J. Magn. Magn. Mater. **14**, 1 (1979).
[46] B. Chen, J. H. Yang, H. D. Wang, M. Imai, H. Ohta, C. Michioka, K. Yoshimura, and M. H. Fang, J. Phys. Soc. Jpn. **82**, 124711 (2013).
[47] J. W. Mayer, M. A. Nicolet, and W. K. Chu, J. Vac. Sci. Technol. **12**, 356 (1975).
[48] L. R. Doolittle, Nucl. Instrum. Methods Phys. Res., Sect. B **9**, 344 (1985).
[49] S. Klotz, J. C. Chervin, P. Munsch, and G. Le Marchand, J. Phys. D: Appl. Phys. **42**, 075413 (2009).